

**Arbeit zur Erlangung des akademischen Grades
Bachelor of Science**

**Search for single top-quark production
in the s-channel with the ATLAS
experiment**

Alfredo Manente
geboren in Dortmund

2025

Lehrstuhl für Experimentelle Physik IV
Fakultät Physik
Technische Universität Dortmund

Erstgutachter: PD Dr. Andrea Helen Knue
Zweitgutachter: Dr. Salvatore La Cagnina
Abgabedatum: 15. Dezember 2025

Kurzfassung

In dieser Arbeit werden Studien zur Messung des Wirkungsquerschnitts für die Erzeugung einzelner Top-Quarks im s-Kanal bei Proton-Proton Kollisionen mit einer Schwerpunktsenergie von $\sqrt{s} = 13 \text{ TeV}$ durchgeführt. Die Daten stammen aus Kollisionsexperimenten des LHC und wurden vom ATLAS Detektor in den Jahren 2015 bis 2018 aufgenommen. Zur Extrahierung des Wirkungsquerschnitts wird ein Profile Likelihood Fit verwendet, wobei als Diskriminante die Ergebnisse eines *Deep Neural Networks*(DNN) fungieren. Die Signal Signatur besteht aus einem geladenen Lepton, entweder Elektron oder Myon, zwei b-tagged Jets und fehlendem transversalen Impuls.

Abstract

The abstract is a short summary of the thesis in English, together with the German summary it has to fit on this page.

Contents

1	Introduction	1
2	Properties of the Top Quark within the Standard Model	2
2.1	Overview of the Standard Model	2
2.2	The Top Quark	4
2.3	Single Top Quark Production in the s-Channel	4
3	The ATLAS Detector	9
4	Object Definition and Event Selection	11
4.1	Monte Carlo Samples	11
4.2	Object Definition	13
4.3	Event Selection	14
5	Analysis and Results	16
5.1	Analysis Strategy	16
5.2	DNN Model	16
5.3	Statistical Method	19
5.4	Systematic Uncertainties	20
5.5	Results	22
6	Summary and Outlook	27
A	Appendix	28
	Bibliography	29

1 Introduction

The Standard Model (SM) of particle physics is the best descriptor for the behaviour of elementary particles and the interactions between them. Despite its major successes many phenomena remain unexplained, like the discovery of the Higgs boson [1, 2] or the top quark [3, 4]. Physics beyond the Standard Model (BSM) is needed to understand the nature of dark matter, neutrino oscillations or the matter-antimatter disbalance. As the heaviest fermion with a mass of about 172.5 GeV [5, 6], the top quark has the strongest coupling to the Higgs field and may act as a potential probe for electroweak symmetry breaking. Therefore it lies potential in uncovering BSM physics. Its short lifetime of $5 \cdot 10^{-25}$ s [7] makes hadronization impossible, which does not enable a direct measurement of the top quark. It almost exclusively decays into a W -boson and a bottom-quark via the weak interaction. In proton-proton (pp) collisions at the Large Hadron Collider (LHC), top-quarks are predominantly produced in top-antitop quark pairs ($t\bar{t}$) via the strong interaction. However, top quarks can be produced singly via the electroweak interaction, with the single-top production in the s- and t-channel, as well as in tW associated production. The s-channel has the smallest cross section of 10.32 pb of all mentioned processes and is dominated heavily by background processes. Unlike the other single top-quark production modes, the s-channel has not yet been measured with a significance over 5σ at the LHC, with the latest ATLAS measurement achieving an observed (expected) significance of 3.3(3.9). [8]. It used a matrix element method (MEM) discriminant in a binned profile likelihood fit to data. Even with its small cross section, the major hindrance in the measurement is the size of the systematic uncertainties. To get a more precise measurement, this thesis will use a more modern approach, with a DNN output as the discriminant for a profile likelihood fit. Simulated data from pp collisions in the LHC at $\sqrt{s} = 13$ TeV measured by the ATLAS detector is used, corresponding to the full Run 2 dataset with a luminosity of 140 fb^{-1} . The structure of this work is as follows: Chapter 2 displays an overview of the SM, the s-channel production mode as well as the dominant backgrounds and the previous measurement. Chapter 3 presents the ATLAS detector. Chapter 4 discusses the simulation, the object definitions and event selections. Chapter 5 describes the main study presented in this thesis. Finally chapter 6 gives a short summary of the results and an outlook to further improvements in the measurement of the single top s-channel.

2 Properties of the Top Quark within the Standard Model

2.1 Overview of the Standard Model

The SM of particle physics is a gauge invariant theory, which describes the fundamental particles and the interactions between them. It was developed throughout the 20th century [9] by combining the discoveries of quantum mechanics and special relativity into a quantum field theory. Three of the four fundamental forces, electromagnetism, the strong interaction and the weak interaction are characterized by it, only excluding gravity. Whereas electromagnetism and gravity act on infinite ranges, the strong and weak force act on subatomic scales.

The SM divides the fundamental particles into two main categories. First fermions, which constitute all known matter and carry half integer spin. Second bosons, which act out the interactions between fermions and carry a whole integer spin. Further, bosons can be divided into vector bosons, with spin 1 and a scalar boson, the Higgs boson (H) with spin 0. The fermions are comprised of quarks and leptons, where both interact with the electromagnetic (EM) force but only quarks experience the strong force. Neutrinos, which take part in the lepton category, only interact via the weak force. The fundamental particles are further split into three generations in relation to their masses and time of discovery. The first generation is comprised of the electron (e) and the corresponding electron neutrino (ν_e) for the lepton part, and the up quark (u) as well as the down quark (d). The second generation leptons include the muon (μ) and the muon neutrino (ν), while the charm quark (c) and the strange quark (s) constitute the second generation quarks. The third generation includes the heaviest fermions, with the tau lepton (τ) and its corresponding tau neutrino (ν_{tau}) on the lepton side and the top quark (t) and bottom quark (b) on the quark side. The electric charge defines the interaction strength with the EM force. All charged leptons posses an electric charge of -1 elementary charge (e). Whereas up-type quarks (u, c, t) carry a charge of $+2/3$ e and down-type quarks (d, s, b) carry a charge of $-1/3$ e. For every fermion there exists an antiparticle counterpart with opposite electric charge and spin. Especially the first generation of fermions constitute to the overwhelming part of matter, where protons and neutrons are build with the u - and d -quarks and electrons as part of atoms.

2.1 Overview of the Standard Model

The force carrying bosons include the photon (γ) for the EM interaction, the W^\pm and Z bosons for the weak interaction and eight gluons with different color for the strong interaction. The photon is mass- and chargeless, with it coupling to every particle possessing an electric charge. The W^\pm and Z bosons of the weak interaction carry relatively high mass, which is the reason for its narrow interaction range. The weak force acts on every fermion, where the W^\pm bosons couple to the weak isospin and the Z boson couples to the weak hypercharge, a combined value of the electric charge and weak isospin. Gluons, mediating the strong interaction, are massless as well and couple to any particle carrying a color charge, either quarks or gluons themselves. There are the three base colors red, green and blue with a respective anticolor counterpart. Gluons always carry two color charges, one base color and one anticolor, resulting in eight different possible permutations. Quarks carry only one color charge. Colour confinement states that every stable composite particle has to be colorless, which is the reason for the finite range of the strong interaction. These stable composites are called hadrons and are further split into mesons and baryons. Mesons are color neutral quark-antiquark pairs. Baryons are color neutral composites of three quarks. The Higgs Boson, proposed by Peter Higgs in 1964 [10], was discovered in 2012 in a combined effort of the ATLAS [1] and CMS [2] experiment at the LHC. As a scalar boson it carries spin 0, no electric charge and is the heaviest boson ($m_H = (125.20 \pm 0.11) \text{ GeV}$ [7]). It mediates none of the fundamental forces, but by coupling to it fermions and the W^\pm and Z boson gain their mass.

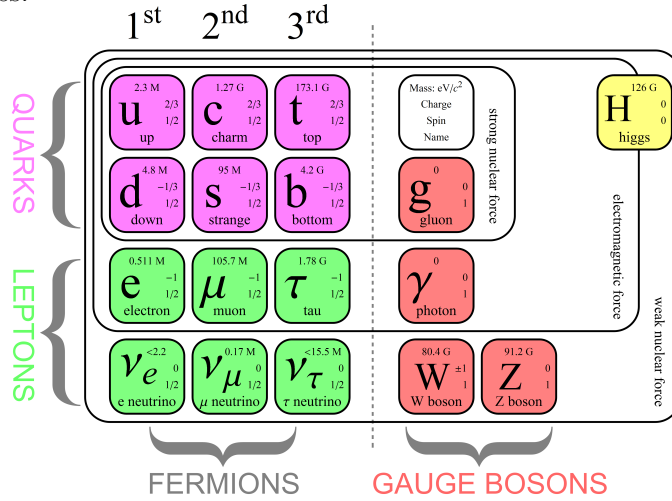


Figure 2.1: The fundamental particles of the Standard Model, showing which forces act on them respectively [11]

2.2 The Top Quark

First postulated by Makoto Kobayashi and Toshihide Maskawa in 1973 [12] and later discovered at Fermilab with the CDF and DØ experiments of the Tevatron collider in 1995 in $p\bar{p}$ collisions [3, 4], the top quark is the last discovered quark in the SM and is the up type quark of the third generation. It carries the heaviest mass of all quarks at $m_t = (172.95 \pm 0.53) \text{ GeV}$ [6] and possesses a large decay width of $\Gamma_t = 1.42^{+0.19}_{-0.15} \text{ GeV}$ [13]. This large decay width leads to a short mean life time of $\tau = \hbar/\Gamma_t \approx 5 \cdot 10^{-25} \text{ s}$ [7]. Unlike other quarks, which hadronize due to color confinement, the top quark decays before hadronization is possible, due to this short lifetime. The top's properties, like spin information or kinematic properties, are then to be decoded by studying the decay particles, which makes its analysis especially interesting. The top quark decays almost exclusively into a W -boson and a b -quark [14].

2.3 Single Top Quark Production in the s-Channel

The s-channel is one of the electroweak top-production modes, producing a single top or antitop quark. In the single top-quark s-channel, a top-quark and a bottom antiquark are created from a virtual W -boson, after the annihilation of a quark and antiquark. The s-channel shows a tWb vertex, with the CKM matrix element being almost one. Therefore the s-channel is a strong probe for the electroweak properties of the top quark. At the LHC, the annihilating particles are predominantly valence up quarks (u) and antidown (\bar{d}) from the pool of sea quarks in the colliding protons.

(Unterschied zwischen \bar{u} und d als annihilierende Teilchen heraus finden)

The Feynman diagram of the s-channel process at LO in QCD is shown in Figure 2.2a.

2.3.1 Top Quark Decay

The top quark decay occurs via the weak interaction, mainly into a b -quark and a W -boson. Furthermore, the W -boson decays either hadronically $2/3$ or leptonically $1/3$ of the time. The hadronic decay results into two quarks, whereas the leptonic decay results in a charged lepton and its corresponding neutrino. The leptonic decay of the W -boson is shown in Figure 2.2b. As there are different color permutations the quarks can carry, the phase space for the hadronic decay is larger, making it

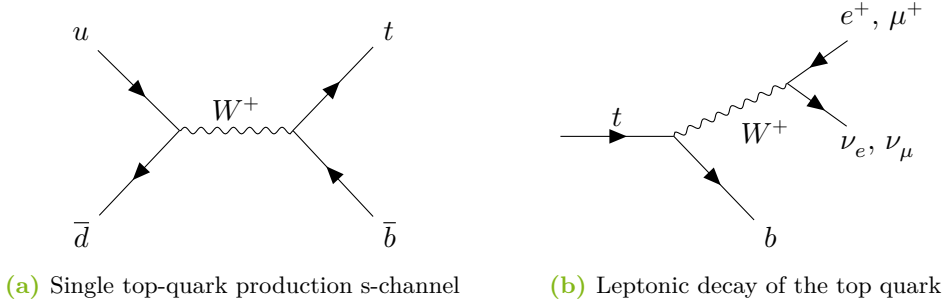


Figure 2.2: Feynman diagram of the single top quark s-channel production mode (left) and the leptonic decay of the top quark (right).

more likely than the leptonic decay. During the s-channel analysis only leptonic W -boson decays are selected, as the final state from the hadronic decay suffers from multijet background production. If the sum of all transverse momenta of all the outgoing particles, does not add to zero, then a particle has remained undetected and the event has missing transverse momentum E_T^{miss} , as prior to the collision. Events with neutrinos in the final state are therefore expected to have missing transverse momentum.

The searched for signature consist therefore of a charged lepton from the leptonic W -boson decay, missing transverse momentum E_T^{miss} from the undetectable neutrino, and two b quarks, one produced from the s-channel process itself and one from the b -quark of the top-quark decay. τ leptons have a short lifetime and can thus not be directly detected, but first and second generation leptons from the τ decay can be observed. Because of that lepton signature is narrowed down to either an electron or muon.

2.3.2 Background Processes

There are physics processes with similar signatures in the detector as the signal process discussed above. Differentiating these processes from the process of interest is a major task in any analysis. These so-called background processes consist predominantly of $t\bar{t}$ production and W +jets production for the single top s-channel analysis. In the LHC collisions, $t\bar{t}$ production occurs mostly through gluon-gluon fusion, but with less probability can also happen through quark-pair-annihilation. With a theoretical cross-section of $\sigma_{t\bar{t}}^{\text{Theo.}} = 832^{+20}_{-29} \text{ pb}$ [15], it exceeds every other top quark production mode. The other single top quark production modes can be mistaken for signal as well, but to a lesser degree, since their cross sections are noticeably smaller than $t\bar{t}$ with $\sigma_{t-\text{chan.}}^{\text{Theo.}} = 216.99^{+9.04}_{-7.71} \text{ pb}$ [**tchan_xsec**] and

$\sigma_{tW\text{-Prod.}}^{\text{Theo.}} = (71.7 \pm 3.8) \text{ pb}$ [tw_xsec]. Other minor backgrounds stem from multijet background processes, $Z+jets$ or diboson(WW, WZ, ZZ) production. Figure 2.3 shows the LO Feynman diagrams for $t\bar{t}$ production via gluon-gluon fusion, and the other two single top-quark production modes.

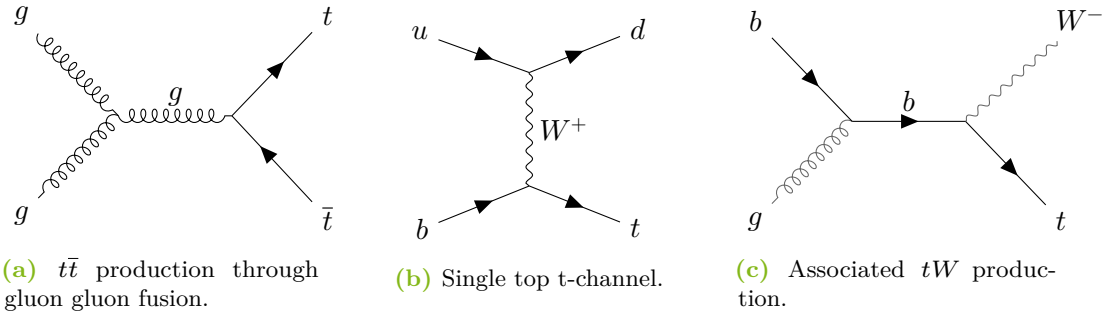


Figure 2.3: Feynman diagrams at LO for the major background processes in the analysis of the single top quark s-channel production mode.

Not only does the $t\bar{t}$ -production mode hold a large cross-section, but the fact that it produces real top-quark decays makes it a difficult background. The two W -bosons, resulting from the t -quark and \bar{t} -quark decay, again can decay leptonically or hadronically. If both W -bosons decay leptonically, the dileptonic final state, can mimic the signal signature if one of the leptons stays undetected. For the semileptonic decay, where one W -boson decays leptonically and one hadronically, the final state signature can emulate the signal if only two b jets get detected. The fully hadronic decay is very unlikely to be mistaken for the signal. Likewise the single top-quark production mode in the t-channel and the associated tW production also show real top quark decays in their signatures. For the t-channel the final state reproduces the signal signature if a b jet or misidentified lighter quark jet gets associated with the event. In the associated tW -production, the b -quark turns into a t -quark by emitting a W -boson. If this W -boson decays hadronically and produces a b jet or a jet that gets misidentified, the final state signature is the same as the signal signature. If the W -boson decays leptonically and two b jets or misidentified jets get associated with the event, the $W+jets$ background also mimics the signal. In the case of multijet background, leptons from heavy flavor decays, electrons from photon conversion or jets misidentified as leptons paired with two b jets or misidentified jets lead to the signal signature.

2.3.3 Previous Measurements

Table 2.1 summarizes the previous measurements of the single top quark s-channel processes taken at the ATLAS detector.

Table 2.1: The three previous measurements of the single top quark s-channel processes taken at the ATLAS detector. Displayed are the cross-sections $\sigma_{s\text{-chan.}}$, the observed (expected) significance and the integrated luminosity for each respective measurement [16, 17, 8].

\sqrt{s}	$\sigma_{s\text{-chan.}}$	$\sigma_{\text{observed}}(\sigma_{\text{expected}})$	L_{int}
7 TeV	$<26.5 \text{ pb}$	—	0.70 fb^{-1}
8 TeV	$4.8 \pm 0.8(\text{stat.})^{+1.6}_{-1.3}(\text{syst.}) \text{ pb}$	$3.2(3.9)$	20.3 fb^{-1}
13 TeV	$8.2 \pm 0.6(\text{stat.})^{+3.4}_{-2.8}(\text{syst.}) \text{ pb}$	$3.3(3.9)$	140 fb^{-1}

The most recent measurement of the s-channel process was done by ATLAS with a center of mass energy of $\sqrt{s} = 13 \text{ TeV}$, with data collected between the years 2015 and 2018, corresponding to the Run 2 dataset at an integrated luminosity of 140 fb^{-1} [8]. The cross section of the measured s-channel resulted in $\sigma_{s\text{-chan.}} = 8.2 \pm 0.6(\text{stat.})^{+3.4}_{-2.8}(\text{syst.}) \text{ pb}$, in comparison to the theoretical estimate of $\sigma_{s\text{-chan.}}^{\text{theo.}} = 10.32^{+0.40}_{-0.36} \text{ pb}$ [`schan_theory_xsec`]. This is equivalent with an observed (expected) signal significance of $3.3(3.9)\sigma$ over the background only hypothesis. The analysis strategy consisted of a preselection and then a split of the events into four categories. First, the so-called signal region (SR), which is enriched with signal events and used to determine the signal strength. Three more control regions are included, depleted in signal events and enriched in background events, to enhance the modelling of the major backgrounds. These are orthogonal, meaning any event gets put only in one of the regions. To extract the signal strength from the events, a profile likelihood fit was done, with a matrix element method (MEM) discriminant. The limiting factors of the previous measurement were noticeably the systematic uncertainties, where $t\bar{t}$ modelling and signal modelling uncertainties, as well as detector modelling uncertainties, had the biggest impact. Table 2.2 displays the systematic uncertainties with the largest percentual impact on the signal strength. The following analysis uses a *Deep Neural Network* discriminant for the profile likelihood fit. As it uses a high-dimensional feature set based on kinematic variables to extract signal from background events, an improvement on the impact of the systematic uncertainties and more precise signal extraction is expected.

Table 2.2: The systematic uncertainties which largest impact on the cross-section measurement of the previous ATLAS measurement of the single top quark s-channel process. The percentual impact of the respective uncertainty on the cross section is shown [8].

Systematic uncertainty	$\frac{\Delta\sigma}{\sigma} [\%]$
$t\bar{t}$ normalisation	+2417
$t\bar{t}$ shape modelling	+1815
s-channel modelling	+188
Jet energy resolution	+1812
Jet energy scale	+1813
MC statistics	+1311
Flavour Tagging	+1210

3 The ATLAS Detector

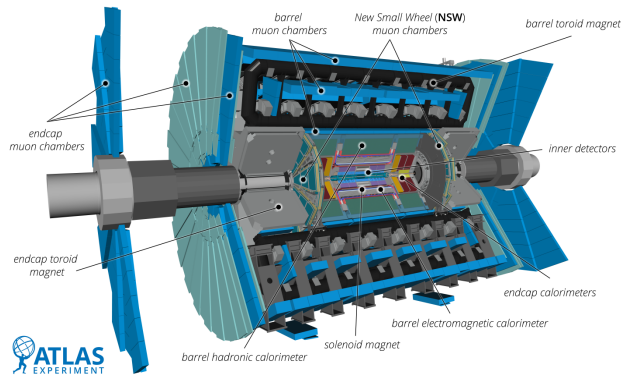


Figure 3.1: Schematic overview of the ATLAS Detector and all its subsystems [18]

As a general purpose detector, the ATLAS detector covers a solid angle range of 4π . The full angular coverage in the beams symmetry plane is granted through its cylindrical design, with a central barrel and two endcaps. It consists of three main subsystems, which are the *Inner Detector* (ID), the *Calorimeter System* and the *Muon Spectrometer* (MS). With the help of a 2 T solenoid magnet, the trajectory of charged particles are bent using the Lorentz force and then reconstructed inside the ID. The calorimeter system consists of an Electromagnetic Calorimeter (ECAL) and Hadronic Calorimeter (HCAL). Inside the ECAL the incoming electrons and photons trigger showers, which ionize parts of the calorimeter and results in energy and direction measurements. Similarly, the HCAL absorbs hadronic jets and triggers hadronic showers, leading to light emissions in the scintillator tubes of the HCAL, from which energy and direction of the jets are determined. As minimal ionizing particles, muons pass all the previously mentioned subsystems and can only be detected in the MS. Here the toroidal magnets in the endcap and barrel parts of the detector bend their tracks and helps in trajectory and charge measurements.

Cartesian coordinates within the LHC are defined as follows: The z -axis is aligned with the beam pipe, the x -axis points to the center of the LHC and the y -axis points upwards to the beam plane. To introduce spherical coordinates, ϕ is used to describe the angle between the y - and x -axis, while θ describes the angle between the y - and

z -axis. Lorentz invariance can then be achieved by introducing the pseudorapidity $\eta = -\ln(\tan \frac{\theta}{2})$. Particle distances within the detector are then defined by the value $\Delta R = \sqrt{\Delta\eta^2 + \Delta\phi^2}$. Transverse momentum is calculated within the cartesian coordinates with $p_T = \sqrt{p_x^2 + p_y^2}$.

4 Object Definition and Event Selection

4.1 Monte Carlo Samples

In order to measure production cross-sections in collision experiments, it is necessary to distinguish the signal process from the various background contributions. In this analysis, the single top quark s-channel production mode is studied, with the dominant background processes being $t\bar{t}$ production, single top quark production in the t-channel, associated tW production, as well as $W+\text{jets}$ and $Z+\text{jets}$ events. The multijet background is estimated using data-driven methods and is therefore not modelled using simulated samples. To compare the observed data with SM predictions and to evaluate detector effects and systematic uncertainties, Monte Carlo (MC) simulations are used. These simulations allow variations of theoretical assumptions and model parameters, in order to provide a detailed description of both signal and background processes. The simulation of particle collisions at high energies is based on the factorization theorem of Quantum Chromodynamics (QCD). According to this theorem, the cross-section of a hadronic process can be factorized into parton distribution functions (PDFs) and a hard scattering matrix element (ME) describing the short-distance interaction. The PDF is a representation of the probability distribution, with which a parton carries a fraction of the momentum of a hadron, denoted by the Bjorken x . $p_i = xp_p$ resembles the momentum fraction the parton i carries from the whole proton momentum p_p . At large momentum transfers, the strong coupling constant α_s is sufficiently small such that the hard scattering can be calculated perturbatively. In this analysis, MEs are calculated at leading order (LO) or next-to-leading order (NLO) in α_s , depending on the process. By convolving the PDFs of the parton constituents i and j with the cross section $\sigma_{ij \rightarrow t\bar{t}}$ of the respective hard scattering sub-process and then summing over all possible sub-processes, the s-channel cross section is determined.

$$\sigma_{\text{s-chan.}} = \sum_{i,j} \int dx_i f_i(x_i, \mu_F^2) \int dx_j f_j(x_j, \mu_F^2) \sigma_{ij \rightarrow t\bar{t}}(\sqrt{s}, m_t, \mu_F, \mu_R, \alpha_S)$$

The formula takes in, the centre-of-mass energy \sqrt{s} of the process, the top quark mass m_t , the coupling strength of the strong interaction α_S , as well as the factorisation scale μ_F and the renormalisation scale μ_R , which are set to the energy scale

of the process. While the hard scattering is accessible to perturbative calculations, subsequent QCD radiation, parton showering and hadronization occur at lower energy scales, where perturbation theory is no longer usable. These effects are therefore modelled using phenomenological models. Parton showers (PS) simulate the emission of soft and collinear radiation, while hadronization models describe the transition from colored partons to colorless hadrons, incorporating the effects of confinement and asymptotic freedom. The free parameters of these models are tuned using experimental data. Several Monte Carlo generators are used in this analysis. POWHEG Box v2 [19, 20, 21] is employed to generate hard scattering processes at NLO accuracy. Parton showering and hadronization are modelled using either PYTHIA 8 [22], which implements the *Lund string model* [23] for hadronization and typically uses the A14 tune [24], or HERWIG 7 [25, 26], which simulates hadronization based on the *cluster hadronization model* [27]. As a general-purpose event generator, SHERPA [28] is capable of simulating both the hard scattering ME and the subsequent PS and hadronization. The decays of heavy-flavour hadrons are simulated using EVTGEN [29], except for samples generated with SHERPA. Throughout all simulations, a top quark mass of 172.5 GeV is used.

For the nominal single top-quark and antitop-quark s-channel samples, POWHEG simulations with the NNPDF3.0NLO PDF set [30] are used, interfaced to PYTHIA used under the *A14* tune. For PS modelling the NNPDF2.3LO [31] PDF set is used. The process is normalized at NLO in QCD to the theoretical cross-section prediction $\sigma_{\text{s-chan.}}^{\text{SM}} = 10.32^{+0.40}_{-0.36} \text{ pb } [\text{ts_xsec}]$.

The t-channel single top-quark and anti-quark processes similarly make use of POWHEG and PYTHIA. The leptonic decay of the W -boson from the top-quark decay is enforced and a Breit-Wigner propagator scheme with a fixed top-quark width of 50 GeV is used. POWHEG uses the NNPDF3.0NLO_nf4 PDF [30] set for ME calculations, while PYTHIA employs the NNPDF2.3LO PDF set for PS modelling. The normalization is based on the cross-section prediction of $\sigma_{\text{t-chan.}}^{\text{SM}} = 217^{+9}_{-8} \text{ pb}$ at NLO in QCD $[\text{t_t_xsec}]$.

Associated tW production samples are generated with POWHEG interfaced with PYTHIA, while further making use of the diagram removal scheme (citation) to handle interference with $t\bar{t}$ production at NLO. Like the signal process, the NNPDF3.0NLO PDF set is used for ME calculations and the NNPDF2.3LO PDF set for PS modelling. The associated tW production is normalized at NLO in QCD to the SM prediction $\sigma_{tW}^{\text{SM}} = (71.7 \pm 3.8) \text{ pb } [\text{tw_xsec}]$.

The $t\bar{t}$ production is utilizing the POWHEG generator at NLO with the NNPDF3.0NLO PDF set, combined with PYTHIA using the NNPDF2.3LO PDF set. The h_{damp} parameter, which regulates the first gluon emission beyond the Born configuration, is set to $1.5 \cdot m_{\text{top}} \simeq 258.75 \text{ GeV}$. The normalization at next-to-next-to-leading order (NNLO) in QCD is calculated to be $\sigma_{t\bar{t}}^{\text{SM}} = 832^{+40}_{-46} \text{ pb}$.

For the $W+jets$ samples the SHERPA 2.2.11 version is used. SHERPA calculates the MEs at NLO accuracy for up to two partons and at LO accuracy for up to five partons, which is combined with PS models. The PS modelling used the NNPDF3.0NNLO PDF set. Normalization at NNLO in QCD is based on $\sigma_{W+jets}^{\text{SM}} = 60.2 \text{ nb}$.

The Drell-Yan production modes of $Z \rightarrow ee$, $Z \rightarrow \mu\mu$, $Z \rightarrow \tau\tau$ are simulated with SHERPA 2.2.11 for the light leptons. For the tau decay SHERPA 2.2.14 with the NNPDF3.0NNLO PDF set is utilized. Similarly MEs are calculated at NLO accuracy for up to two partons and at LO accuracy for up to five partons. The process is normalized at NNLO accuracy in QCD to $\sigma_{Z+jets}^{\text{SM}} = 6.32 \text{ nb}$.

All nominal samples were simulated using the full ATLAS detector simulation [32] based on GEANT4 [33], hereafter referred to as *fullsim*. Some alternative samples use a faster simulation procedure, where the GEANT4 simulation of the calorimeter response is replaced by a detailed parameterisation of the PS shapes [32], in the following referred to as *fastsim*.

4.2 Object Definition

The signal signature consists of a charged lepton (electron or muon), its corresponding neutrino, and jets originating from b quarks, so-called b -tagged jets. Due to color confinement, quarks hadronize and are reconstructed as jets. The flavor of a jet cannot be measured directly and is inferred using dedicated flavor-tagging algorithms. The following framework is used to define the object reconstruction in this analysis.

Electrons are reconstructed from charged-particle tracks in the ID matched to energy deposits in the ECAL. They are required to have a transverse momentum of $p_T > 10 \text{ GeV}$ and a pseudorapidity of $|\eta_{\text{cluster}}| < 2.47$, excluding the barrel-endcap transition region $1.36 < |\eta_{\text{cluster}}| < 1.52$. Electrons must satisfy the `TightLH` identification and the tight isolation working point [34]. Muons are reconstructed by combining tracks from the ID and the MS. They are required to have $p_T > 10 \text{ GeV}$ and $|\eta| < 2.5$, and must pass the medium quality selection and the tight isolation working point [35]. To ensure consistency with the primary interaction, lepton tracks are required to originate from the primary vertex by satisfying $|z_0 \sin \theta| < 0.5 \text{ mm}$ and $|d_0/\sigma(d_0)| < 5$ (3) for electrons (muons), where z_0 is the longitudinal impact parameter and d_0 the transverse impact parameter with respect to the beam line. Jets are reconstructed using the anti- k_t algorithm [36, 37] with a radius parameter of $R = 0.4$. Jets originating from the hard-scatter interaction are identified using the Jet Vertex Tagger (JVT) [38], while forward jets ($|\eta| > 2.5$) are validated using the forward JVT (fJVT) algorithm [39]. Jets containing b hadrons are identified using the GN2v01 b -tagging algorithm [40, 41, 42, 43]. The algorithm assigns a continuous discriminant to each jet, representing the likelihood of originating from

a b quark. A working point corresponding to a b -jet identification efficiency of 85% is applied. The discriminant exploits the long lifetime of b hadrons, leading to displaced decay vertices and tracks with large impact parameters.

4.3 Event Selection

A dedicated event selection is applied to obtain a signal-enriched sample targeting the single top-quark s-channel signature, characterized by one charged lepton (electron or muon), missing transverse momentum E_T^{miss} from the neutrino, and two b -tagged jets. Events are required to pass a pre-selection consisting of exactly one isolated lepton with $p_T > 28 \text{ GeV}$ and at least two b -tagged jets with $p_T > 20 \text{ GeV}$, where at least one jet must satisfy the 85% b -tagging working point. The final selection defines the signal region (SR). Events must contain exactly one isolated lepton with $p_T > 30 \text{ GeV}$ and exactly two central jets ($|\eta| < 2.5$), both fulfilling the 77% b -tagging working point. The leading (subleading) jet is required to have $p_T > 40 \text{ GeV}$ (30 GeV). Furthermore, $E_T^{\text{miss}} > 35 \text{ GeV}$ and the transverse mass of the W boson,

$$m_T^W = \sqrt{2p_T^l E_T^{\text{miss}} (1 - \cos \Delta\phi(l, E_T^{\text{miss}}))},$$

is required to exceed 30 GeV, effectively suppressing multijet background contributions. Additional vetoes are applied to further reduce background contamination. Events containing extra jets with $p_T > 30 \text{ GeV}$ or forward jets ($|\eta| > 2.5$) are rejected, significantly reducing the single top quark t-channel background. Events with additional low transverse momentum leptons are vetoed to suppress multilepton backgrounds. All selection criteria defining the signal region are summarized in Table 4.1.

Table 4.1: Definition of the event selection for the Signal Region (SR) used in this analysis.

	SR
$N(e, \mu)$	≥ 1 with $p_T > 30 \text{ GeV}$
$N(\text{jets})$	≥ 2 , in $ \eta < 2.5$
$N(b - \text{tags})$	≥ 2 , @77%, in $ \eta < 2.5$
Leading jet p_T	$> 40 \text{ GeV}$, in $ \eta < 2.5$
Subleading jet p_T	$> 30 \text{ GeV}$, in $ \eta < 2.5$
Missing transverse momentum (E_T^{miss})	$> 35 \text{ GeV}$
Transverse W boson mass (m_T^W)	$> 30 \text{ GeV}$
Additional jets (low p_T) veto	No jets with $p_T < 30 \text{ GeV}$
Forward jets veto	No jets with $ \eta > 2.5$
Additional leptons veto	No extra leptons with $p_T < 30 \text{ GeV}$

Table 4.2: blabla

Process	$L_{\text{int}} \cdot \sigma_i$	Number of events
s-channel	$461 \cdot 10^3$	4139.99 ± 850.839
t-channel	$6.28 \cdot 10^6$	9334.36 ± 1853.71
tW production	$10.1 \cdot 10^6$	2619.05 ± 612.957
$Z + \text{jets}$		1654.39 ± 882.368
$W + \text{jets}$		15159.5 ± 7858.56
$t\bar{t}$	$102 \cdot 10^6$	75216.7 ± 18753.3
Total		108124 ± 24971.1

5 Analysis and Results

5.1 Analysis Strategy

Throughout this analysis, steps are taken to determine the signal strength $\mu_{\text{s-chan.}} = \sigma_{\text{s-chan.}}^{\text{measured}} / \sigma_{\text{s-chan.}}^{\text{theory}}$ of the single top quark s-channel process. This is done via a binned likelihood fit, where a *Deep Neural Network* (DNN) output is used as discriminant value, to discern signal events from background events. Only one signal region, passing the event selection in Table 4.1, is defined in this thesis. As systematic uncertainties are the limiting factors in the search for the single top quark s-channel process, the systematics with the biggest impact are further inspected and discussed.

5.2 DNN Model

The single top quark s-channel process is dominated by large backgrounds. Extracting signal events from this large background is rather difficult. To achieve an optimal separation between signal and background, a multivariate approach that exploits as much kinematic information as possible is required. For this reason, a DNN classification will be used as the discriminant variable in the binned likelihood fit. The DNN used in this analysis was designed by Niklas Düser as part of his Master's Thesis at the *Technische Universität Dortmund* [44]. It makes use of several high-level kinematic variables to distinguish signal events from background events. The network architecture consists of an input layer with 128 nodes, followed by four hidden layers with 256, 64, 32 and 16 nodes, respectively. The model was trained using the KERAS API within the TENSORFLOW framework [45, 46], employing the binary cross-entropy loss function and the Adam optimizer [47]. For the training and validation datasets, the single top quark s-channel events were used as signal. While the $t\bar{t}$ process, the single top quark t-channel and associated tW production processes, as well as the $W+\text{jets}$ and $Z+\text{jets}$ processes constitute the background. The training samples correspond to an integrated luminosity of 28 fb^{-1} . For every single particle that gets reconstructed, the kinematic variables p_T, η, φ and the invariant mass m get included as features for the DNN model. For particle pairs their pseudorapidity difference $\Delta\eta$ and the difference in the azimuthal angle $\Delta\varphi$

is incorporated as a feature. From the detector measurements of the final state particles, every other particle can be retraced up to the virtual W -boson. First, the final state lepton and corresponding neutrino are reproduced. From the condition that the leptons and the neutrinos momentum squared must equal the invariant mass of the decaying W_{Decay} -boson the neutrino four-momentum is reconstructed. With the lepton and neutrino reconstructed, the top quark mass can be calculated. With information about the leading b -tagged jet and the W_{Decay} -boson, the top quark can be reconstructed. The top quark four-momentum and the second b -tagged jet are then used to reconstruct the virtual $W_{\text{Prod.}}$ -boson. The transverse mass of the W_{Decay} -boson m_T^W and the missing transverse momentum E_T^{miss} of the event are included as feature. The transverse mass of the top quark, defined as $m_T^{\text{top}} = \sqrt{E_{T,\text{sum.}}^2 - p_{T,\text{sum.}}^2}$, with the sums of the transverse energies and transverse momenta of the top quarks decay particles, is also used. The scalar sum of the transverse energies of all final-state particles is called H_T , whereas $H_{T,\text{had.}}$ and $H_{T,\text{lep}}$ sum only over the transverse energies of the final state hadrons or leptons respectively. Another set of event shape variables are inferred through the momentum tensor, that encodes the high-levels momentum distributions of the reconstructed objects. Its elements are derived by the formulae

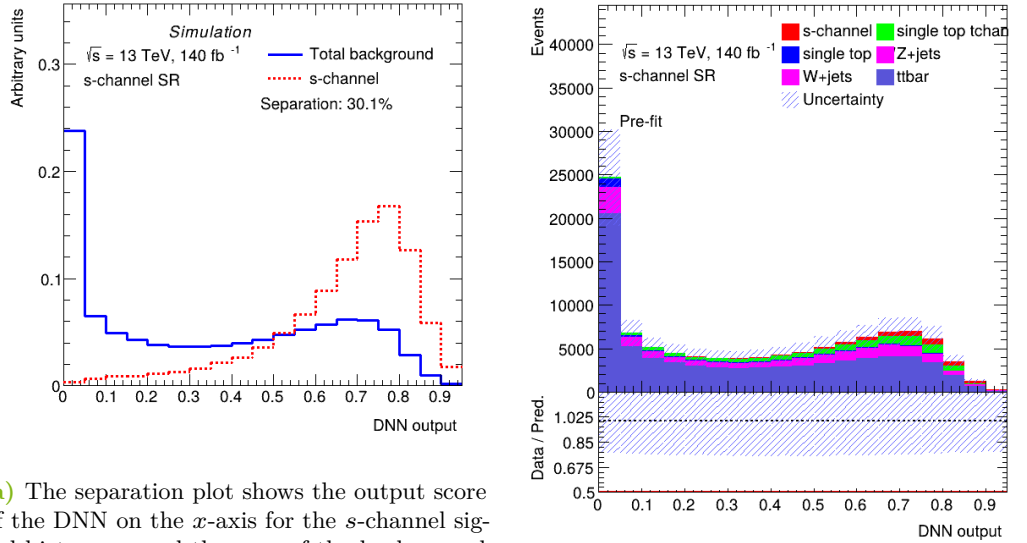
$$M_{ij} = \frac{\sum_{k=1}^N p_{k,i} p_{k,j}}{\sum_{k=1}^N p_k^2}, \quad i, j \in x, y, z$$

by summing over all final-state particles, where $p_{k,i}$ denotes the i -th component of the k -th final state particle. Through the sorted eigenvalues of the momentum tensor $\lambda_0 > \lambda_1 > \lambda_2$ further event variables are constructed:

Aplanarity :	$\mathcal{A} = \frac{3\lambda_2}{2},$
Planarity :	$\mathcal{P} = \frac{3(\lambda_2 + \lambda_1)}{2},$
Sphericity :	$\mathcal{S} = \lambda_1 - \lambda_2.$

The DNN is applied to all signal and background events in the SR. The corresponding distributions are shown in Figure 5.1. Figure 5.1a shows signal and background normalized to the same integral, to show the achieved separation of the classifier. The combined DNN output histograms of each respective process is shown in Figure 5.1b.

5 Analysis and Results



(a) The separation plot shows the output score of the DNN on the x -axis for the *s*-channel signal histogram and the sum of the background histograms. Both histograms are normalised. A separation of 30.1% is achieved, displayed by the observably separated peaks with yet significant overlap of both distributions.

(b) The combined DNN output for every process of interest in this analysis. Histograms are stacked, where the signal events are displayed in red on the top of the stack.

Figure 5.1: The DNNs output is shown with a separation plot and the combined DNN output for the different processes.

5.3 Statistical Method

With the neural network output x as the discriminant, the expected number of events in the i -th bin $\lambda_i(\mu, \theta) = \mu \cdot s_i(\theta) + b_i(\theta)$ is used to incorporate the signal strength. Here $s_i(\theta)$ and $b_i(\theta)$ signify the expected signal and background contributions respectively, which are obtained by processing the simulated signal and background events through the trained DNN model and evaluating the corresponding output score x . The parameter μ represents the signal strength and scales the overall signal contribution uniformly across all bins, while the nuisance parameters (NPs) θ encode the effect of systematic uncertainties on both the normalization and the shape of the signal and background distributions. To determine the cross-section, a *binned profile likelihood fit* is performed with the HISTFACTORY tool [48]. This framework is used to extract the signal strength parameter μ together with the NPs describing systematic uncertainties by maximizing the likelihood function. This determines the parameter values that best describe the data assuming the presence of the single top quark s-channel signal. The likelihood function states the probability by which an outcome happens with respect to a set of given model parameters. Since analyses in High Energy Physics involve large event samples, the data are represented in histograms, where events are grouped into bins rather than treated individually. The binning of data also introduces Poisson probabilities into the likelihood as can be seen in the following equation:

$$\mathcal{L}(\mu, \theta) = \prod_{i=1}^{N_{\text{bins}}} \text{Pois}(n_i | \lambda_i(\mu, \theta)) \cdot \prod_{j=1}^{N_{\text{NP}}} \pi_j(\theta_j) .$$

The binned likelihood function multiplies the Poisson probabilities $\text{Pois}(n|\lambda)$ in each bin, which state the probability of observing n events under the expectation λ

$$\text{Pois}(n|\lambda) = \frac{\lambda^n e^{-\lambda}}{n!},$$

multiplied with the product of all constraint terms $\pi_j(\theta_j)$ for each NP j . A NP of $\theta_j = 0$ conforms to the nominal prediction made by the simulation, while $\theta_j = \pm 1$ represents a variation of one standard deviation $\pm \sigma$. For most systematic uncertainties, the constraint terms are modelled as Gaussian distributions centered at the nominal value θ_j^0 with a width corresponding to the estimated uncertainty σ_{θ_j} . The one standard deviation variations are provided in the form of up and down shifted histograms. Statistical uncertainties arising from the limited number of simulated events are included as dedicated NPs γ_i for each respective bin i , which are modelled as Poisson-constrained parameters with a nominal value of

5 Analysis and Results

1. By maximizing the likelihood function via variation of the parameters μ and θ_j , their final values are determined by $\hat{\mu}, \hat{\theta} = \underset{\mu, \theta}{\operatorname{argmax}} \mathcal{L}(\mu, \theta)$. In practice, the negative logarithm of the likelihood function $-\ln \mathcal{L}$ is minimized, as the maximum is unaffected by taking the logarithm and the multiplications are transformed into sums. Summing over the logarithms and minimizing is computationally more robust. The negative log-likelihood (NLL) function is minimized with MINUIT [49]. The signal strength μ and all NPs can vary while fitting. μ is free-floating, while the NPs are penalized based on their respective uncertainties. If after the fit the uncertainty of a NP is smaller than the provided uncertainty $\sigma_{\theta_j^0}$, the fit achieved a constraint on the respective systematic uncertainty.

To assess the expected sensitivity of the analysis and study the impact of systematic uncertainties in the absence of statistical fluctuations, an *Asimov fit* is performed. The *Asimov dataset* is constructed by replacing the observed event counts in each bin with their expected values under the nominal SM predictions. The Asimov fit provides the expected best-fit values and uncertainties of the signal strength and nuisance parameters, assuming perfect agreement between data and the model.

5.4 Systematic Uncertainties

The systematic uncertainties are categorized into modelling uncertainties of the single top quark s-channel signal process, background modelling uncertainties with a particular focus on the $t\bar{t}$ process, and detector modelling uncertainties.

Modelling uncertainties arise from different theoretical descriptions of the hard-scattering process and its subsequent evolution, including variations in ME calculations, PS modelling, hadronization, and the choice of generator-specific parameters. For the single top quark s-channel signal process, additional MC samples were produced by varying the p_T^{hard} parameter to 1, compared to the nominal value of 0. The p_T^{hard} variable determines how the event hardness calculated by POWHEG is passed to PYTHIA to regulate the parton shower. By default, the hardness scale *SCALUP* provided by POWHEG is used directly. When setting $p_T^{\text{hard}} = 1$, the event hardness is instead defined by the transverse momentum of the hardest POWHEG emission [50]. This variation probes uncertainties related to the matching between the NLO matrix element and the PS. In addition, samples interfacing POWHEG with HERWIG were generated to assess uncertainties originating from different parton shower and hadronization models. Similar modelling variations were applied to the $t\bar{t}$ background process. Further $t\bar{t}$ samples were produced with $p_T^{\text{hard}} = 1$, and with the h_{damp} parameter increased from $1.5 \cdot m_{\text{top}}$ to $3 \cdot m_{\text{top}}$, allowing the

study of uncertainties related to the modelling of high- p_T radiation in the hardest emissions.

In addition to ME and PS modelling uncertainties, background processes are subject to uncertainties in their theoretical cross-section predictions, which affect their normalisation. A cross-section uncertainty of 6% is assigned to the $t\bar{t}$ background and to the single top quark production modes. For the $W+\text{jets}$ and $Z+\text{jets}$ background processes, a conservative uncertainty of 50% is assumed.

Detector modelling uncertainties include both one-sided and two-sided systematic variations. Two-sided systematics are provided with independent up and down variations, while one-sided systematics are symmetrised with respect to the nominal distribution. The latter include uncertainties on the missing transverse momentum E_T^{miss} , parametrising the resolution of the Track Soft Term (TST) in directions parallel and perpendicular to the hard-scatter axis. The integrated luminosity uncertainty is taken to be 0.83% [51]. Jet-related uncertainties include jet energy resolution (JER), jet vertex tagger (JVT), and jet energy scale (JES) uncertainties. The JER uncertainty is represented by 15 NPs, while two efficiency-related nuisance parameters are used for JVT. The JES uncertainty accounts for effects related to jet flavour composition, flavour response, b -jet energy scale, pile-up, punch-through, and jet η intercalibration, as well as various pre-recommendations, and is encoded using 32 nuisance parameters. Flavour tagging uncertainties are modelled using 55 nuisance parameters for b -tagging, 33 for c -tagging, and 42 for light-flavour jet tagging. In addition, four nuisance parameters per flavour are included to describe uncertainties arising from the extrapolation of the jet calibration to the high transverse momentum regime, where direct experimental constraints are limited. Uncertainties related to the modelling of electrons and muons are also considered. For electrons, six nuisance parameters are included, covering trigger efficiencies as well as energy scale and resolution effects for electrons and photons. For muons, 16 nuisance parameters are used to describe momentum scale and resolution uncertainties, as well as trigger-related effects. The uncertainty associated with pile-up reweighting is represented by a single nuisance parameter.

Additional theoretical uncertainties affecting both the single top quark s-channel signal and the $t\bar{t}$ background arise from variations of the renormalisation and factorisation scales, as well as from initial- and final-state radiation modelling.

In order to be less dependent on statistical fluctuations, the systematics distributions are smoothed. For uncertainties containing an up and down variation, two-sided symmetrization is applied. The up and down variation for each respective bin i consists therefore of the mean of both, given by $\pm \frac{n_i^{\text{up}} - n_i^{\text{down}}}{2}$. Uncertainties with

5 Analysis and Results

only an up or down variation undergo one-sided symmetrisation, in which the existing variation is mirrored for the missing counterpart.

5.5 Results

After fitting the NLL onto the Asimov Dataset, the expected signal strength is found to be $\mu_{s\text{-chan.}} = 1^{+0.25}_{-0.20}$. The DNNs output is therefore still consistent with the SM prediction, even after incorporating several more systematic uncertainties into this analysis, as were considered in Niklas Düser's work. From the fit the NPs influences on the signal strength are now accessible. The ranking plot sorts the NPs, with the most influential NP shown on the top of the plot, based on their impact on the signal strength. Their respective impacts are calculated using the *covariance matrix method* [52]. Here the impact $I = \sigma_{\text{total}}^\mu C_{\mu,\text{NP}} \sigma^{\text{NP}}$ is determined with the correlation $C_{\mu,\text{NP}}$ between the signal strength and the respective NP, the total uncertainty $\sigma_{\text{total}}^\mu$ of the signal strength and the uncertainty σ^{NP} of the NP. The ranking therefore reflects the sensitivity of the analysis to variations of individual nuisance parameters and provides insight into the dominant sources of systematic uncertainty. The ranking plot for this analysis is displayed in Figure 5.2

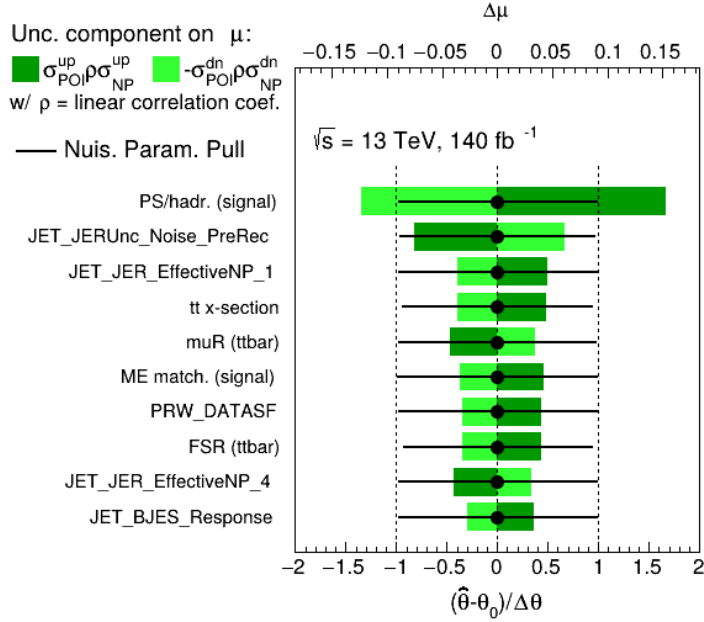


Figure 5.2: The ranking plot sorts the NPs from top to bottom regarding their impact on the signal strength.

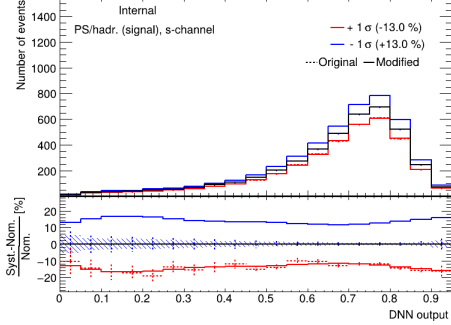
The ranking plot reveals that the dominant uncertainty originates from the PS and hadronization modelling of the single top quark s-channel signal process. This is expected, as the hadronic signature of the signal consists only of two b -tagged jets, whose relative kinematics are strongly influenced by the modelling of hard emissions and subsequent showering. The leading and subleading jet transverse momenta are the most impactful input features of the DNN, as seen in section 5.2. This explains the strong sensitivity to PS and hadronization uncertainties, as these directly affect the jet kinematics exploited by the classifier. On detector level, jet energy resolution uncertainties, in particular the noise pre-recommendation uncertainty and the effective NP 1 uncertainty, have a sizable impact. These uncertainties affect the reconstructed jet momenta and therefore propagate directly to high-level kinematic variables used by the DNN. Uncertainties related to the modelling of the $t\bar{t}$ background, including the theoretical prior on the $t\bar{t}$ cross-section and the renormalisation scale uncertainty μ_R , also show a significant impact. As $t\bar{t}$ constitutes the dominant background process and the signal-to-background ratio of the single top s -channel is small, the analysis is particularly sensitive to variations in the $t\bar{t}$ kinematic description. In particular, variations of the renormalisation scale affect the amount of QCD radiation in the $t\bar{t}$ process, leading to altered jet multiplicities and kinematic distributions, which in turn influence the DNN output. In addition to parton shower and hadronization uncertainties, the ME matching uncertainty exhibits a strong impact on the extracted signal strength. The ME matching procedure governs the transition between hard emissions described by the fixed-order matrix element and soft or collinear radiation modelled by the PS. For the single top quark s-channel process, which is characterised by a very simple hadronic final state consisting of only two b -tagged jets, the modelling of additional radiation plays a particularly important role. Variations in the ME matching scheme affect the jet multiplicity as well as the transverse momentum and angular correlations of the b -jets. Since the DNN relies strongly on jet-related high-level kinematic variables, these modelling differences propagate directly to the classifier output, leading to a sizeable shape effect. Moreover, the ME matching uncertainty cannot be efficiently constrained by the fit, as it does not primarily affect the overall normalisation but rather the kinematic structure of the signal events. Pile-up refers to additional pp interactions occurring in the same or neighbouring bunch crossings as the hard-scatter event. These interactions introduce extra tracks and energy deposits in the detector, which can bias the reconstruction of jets, missing transverse momentum and other event-level observables. Uncertainties related to pile-up reweighting therefore affect jet multiplicities, jet energies and several high-level kinematic variables, and consequently propagate to the DNN classification. Final State Radiation (FSR) uncertainties of the $t\bar{t}$ background process similarly influence hadronic signatures from the major background source. The remaining JER and JES uncertainties also effect the jet reconstruction on the detector level.

5 Analysis and Results

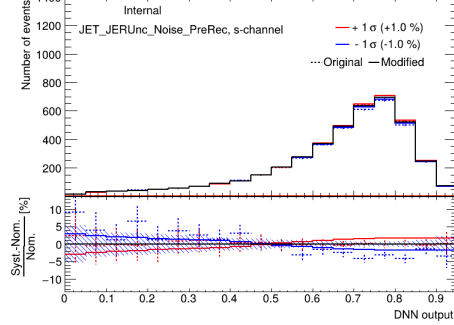
Overall, the dominant uncertainties are those affecting the kinematic properties of jets and the modelling of QCD radiation, highlighting the strong interplay between the DNN-based event classification and the theoretical and detector-level description of jet-related observables. Ratio plots of the uncertainties discussed in detail are shown in Figure 5.3. These plots show the relative variation of a given observable under the up- and down-variations of a NP with respect to the nominal prediction.

The overall impact of systematic uncertainties is reduced in this analysis compared to the previous measurement. This improvement is illustrated in Table 5.1, which shows the percentage impact of the systematic uncertainties grouped by categories. For the comparison of the impact of systematic uncertainties between analyses, the category-wise impacts were determined. All nuisance parameters within a given category were fixed and then fitted, and the resulting change in the signal strength was compared to the nominal full fit.

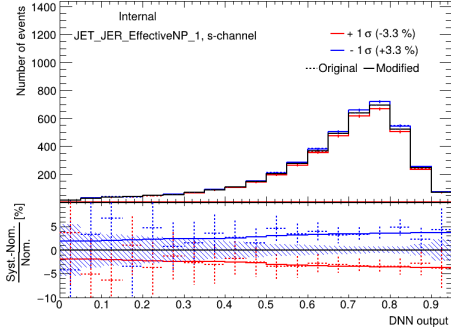
The reduction of the uncertainties can be attributed to the DNN’s ability to exploit a large set of high-level kinematic features and to capture non-linear correlations between them. In contrast, the MEM is limited to a smaller set of observables and simplified correlations, which makes it more sensitive to individual variations in the input distributions. In addition, several systematic uncertainties have been refined since the previous measurement. The ME matching uncertainty for the respective MC samples has been updated, the JER uncertainty now includes a larger set of effective nuisance parameters, and the JES uncertainty benefits from the introduction of a pre-recommendation. These uncertainties directly affect the high-level kinematic variables used as input features in the DNN, such as the transverse momenta of the leading and subleading jets and the event-level correlations between them. By providing a more detailed and accurate modelling of these effects, the improved uncertainties reduce unrealistic variations in the input features, which in turn leads to a smaller propagated impact on the DNN classification and the measured signal strength.



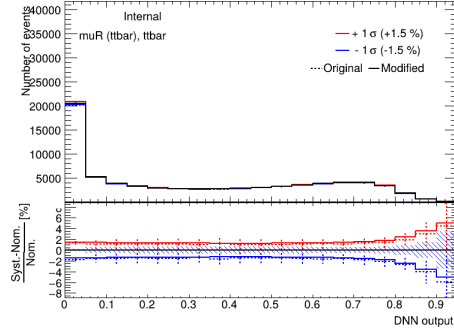
(a) PS and hadronization modelling uncertainty for the signal process.



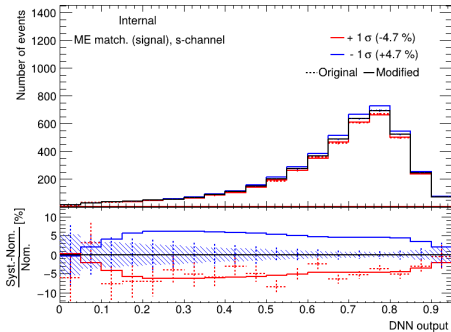
(b) The jet energy resolution noise pre-recommendation uncertainty for the signal process.



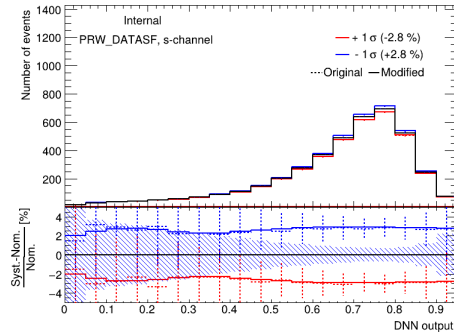
(c) The jet energy resolution effective NP 1 uncertainty for the signal process.



(d) Uncertainty for the renormalisation factor μ_R for the $t\bar{t}$ background process.



(e) ME matching uncertainty for the signal process.



(f) The pile-up reweighting uncertainty for the signal process.

Figure 5.3: Ratio plots for the six uncertainties with the largest impact on the signal strength in this analysis. The upper pad of each plot displays the nominal distribution together with the up- and down-variations, while the lower pad shows the ratio.

Table 5.1: Category-wise impact of systematic uncertainties on the fitted signal strength. Systematic uncertainties of this analysis are compared with the impacts in the previous measurement, taken from [8].

Systematic	Previous measurement: $\frac{\Delta\mu}{\mu} [\%]$	Current measurement $\frac{\Delta\mu}{\mu} [\%]$
s-channel modelling	+18/ - 8	+2/ - 2
$t\bar{t}$ shape modelling	+18/ - 15	+6/ - 5
Jet Energy Resolution	+18/ - 12	+11/ - 9
Jet Energy Scale	+18/ - 13	+5/ - 4
Jet Vertex Tagger	-	+1/ - 1
MC statistics	+13/ - 11	+1/ - 1
Flavor Tagging	+12/ - 10	+4/ - 4
Luminosity	+4/ - 3	+1/ - 1
Pile-up Reweighting	+5/ - 3	+4/ - 3
Electron	-	+1/ - 1
Muon	-	+1/ - 1
Missing Transverse Momentum	+1/ - 1	+5/ - 4
Background Normalisation	-	+20/ - 13
Systematic uncertainties	+42/ - 34	+21/ - 19
Statistical uncertainties	+8/ - 8	+12/ - 6
Total	+42/ - 35	+25/ - 20

6 Summary and Outlook

A study of the impact of systematic uncertainties on the signal strength $\mu_{\text{s-chan.}}$ of the single top quark s-channel process was performed, as previous measurements were limited by these uncertainties. Monte Carlo simulations corresponding to the Run2 dataset, collected between 2015 - 2018 at $\sqrt{s} = 13 \text{ TeV}$ with the ATLAS detector, were used. Only the leptonic decay mode of the W -boson from the top quark decay was considered, resulting in a signal signature consisting of exactly one charged lepton, the corresponding neutrino inferred from the missing transverse momentum E_T^{miss} , and two b-tagged jets. As the statistical method, a binned profile likelihood fit was performed on an Asimov dataset using a single signal region. The output of a deep neural network was employed as the discriminant variable. The fitted singal strength was found to be $\mu_{\text{s-chan.}} = 1^{+0.25}_{-0.20}$. The systematic uncertainties with the largest impact on the signal strength were discussed. The dominant contributions originate from PS and hadronisation modelling of the single top quark s-channel signal process, jet energy resolution uncertainties at detector level, background modelling uncertainties of the dominant $t\bar{t}$ background, and uncertainties related to pile-up reweighting. Compared to the MEM discriminant used in the previous analysis, the use of the DNN output as discriminant significantly reduces the overall impact of systematic uncertainties on the extracted signal strength.

The following elements represent next steps for future analyses: Adding the remaining uncertainties, especially the PDF uncertainties. These can affect the DNN classification through their impact on the high-level kinematic variables used as input features, especially in regions of high momentum transfer. Furthermore the inclusion of orthogonal control regions rich in background events, to enable a more data driven constraint of modelling and normalisation uncertainties of the background processes. This approach enables the background normalisation factors to be treated as free parameters in the fit and constrained by data rather than relying solely on theoretical cross-section uncertainties. Additionally, the use of a more stringent b -tagging working point can reduce mistag contributions and improve the purity of the events classified as signal. Finally, performing a fit to data allows for a validation of the analysis strategy and demonstrates the improved discriminating power of the DNN output when used as the discriminant variable.

A Appendix

Hier könnte ein Anhang stehen, falls Sie z. B. Code, Konstruktionszeichnungen oder Ähnliches mit in die Arbeit bringen wollen. Im Normalfall stehen jedoch alle Ihre Resultate im Hauptteil der Bachelorarbeit und ein Anhang ist überflüssig.

Bibliography

- [1] ATLAS Collaboration. “Observation of a new particle in the search for the Standard Model Higgs boson with the ATLAS detector at the LHC.” In: *Physics Letters B* 716.1 (2012), pp. 1–29. ISSN: 0370-2693. DOI: <https://doi.org/10.1016/j.physletb.2012.08.020>. URL: <https://www.sciencedirect.com/science/article/pii/S037026931200857X>.
- [2] CMS Collaboration. “Observation of a new boson at a mass of 125 GeV with the CMS experiment at the LHC.” In: *Physics Letters B* 716.1 (2012), pp. 30–61. ISSN: 0370-2693. DOI: <https://doi.org/10.1016/j.physletb.2012.08.021>. URL: <https://www.sciencedirect.com/science/article/pii/S0370269312008581>.
- [3] DØCollaboration. “Observation of the Top Quark.” In: *Phys. Rev. Lett.* 74 (14 Apr. 1995), pp. 2632–2637. DOI: [10.1103/PhysRevLett.74.2632](https://doi.org/10.1103/PhysRevLett.74.2632). URL: <https://link.aps.org/doi/10.1103/PhysRevLett.74.2632>.
- [4] F. Abe et al. “Observation of Top Quark Production in $\bar{p}p$ Collisions with the Collider Detector at Fermilab.” In: *Phys. Rev. Lett.* 74 (14 Apr. 1995), pp. 2626–2631. DOI: [10.1103/PhysRevLett.74.2626](https://doi.org/10.1103/PhysRevLett.74.2626). URL: <https://link.aps.org/doi/10.1103/PhysRevLett.74.2626>.
- [5] ATLAS Collaboration. “Combination of Measurements of the Top Quark Mass from Data Collected by the ATLAS and CMS Experiments at $\sqrt{s} = 7\text{ TeV}$ and 8 TeV .” In: *Physical Review Letters* 132.26 (June 2024). ISSN: 1079-7114. DOI: [10.1103/physrevlett.132.261902](https://doi.org/10.1103/physrevlett.132.261902). URL: <http://dx.doi.org/10.1103/PhysRevLett.132.261902>.
- [6] ATLAS Collaboration. “Measurement of the top quark mass with the ATLAS detector using $t\bar{t}$ events with a high transverse momentum top quark.” In: *Physics Letters B* 867 (Aug. 2025). ISSN: 0370-2693. DOI: [10.1016/j.physletb.2025.139608](https://doi.org/10.1016/j.physletb.2025.139608). URL: <http://dx.doi.org/10.1016/j.physletb.2025.139608>.
- [7] S. Navas et al. “Review of Particle Physics.” In: *Phys. Rev. D* 110 (3 Aug. 2024), p. 030001. DOI: [10.1103/PhysRevD.110.030001](https://doi.org/10.1103/PhysRevD.110.030001). URL: <https://link.aps.org/doi/10.1103/PhysRevD.110.030001>.

Bibliography

- [8] ATLAS Collaboration. “Measurement of single top-quark production in the s-channel in proton–proton collisions at $\sqrt{s} = 13$ TeV with the ATLAS detector.” In: *Journal of High Energy Physics* 2023.6 (2023). ISSN: 1029-8479. DOI: 10.1007/jhep06(2023)191. URL: [http://dx.doi.org/10.1007/JHEP06\(2023\)191](http://dx.doi.org/10.1007/JHEP06(2023)191).
- [9] Mary K. Gaillard, Paul D. Grannis, and Frank J. Sciulli. “The standard model of particle physics.” In: *Reviews of Modern Physics* 71.2 (Mar. 1999), S96–S111. ISSN: 1539-0756. DOI: 10.1103/revmodphys.71.s96. URL: <http://dx.doi.org/10.1103/RevModPhys.71.S96>.
- [10] Peter W. Higgs. “Broken Symmetries and the Masses of Gauge Bosons.” In: *Phys. Rev. Lett.* 13 (16 Oct. 1964), pp. 508–509. DOI: 10.1103/PhysRevLett.13.508. URL: <https://link.aps.org/doi/10.1103/PhysRevLett.13.508>.
- [11] Nicola Serra. *Standard Model*. 2025. URL: <https://www.physik.uzh.ch/groups/serra/StandardModel.html>.
- [12] Makoto Kobayashi and Toshihide Maskawa. “CP-Violation in the Renormalizable Theory of Weak Interaction.” In: *Progress of Theoretical Physics* 49.2 (Feb. 1973), pp. 652–657. DOI: 10.1143/PTP.49.652. eprint: <https://academic.oup.com/ptp/article-pdf/49/2/652/5257692/49-2-652.pdf>. URL: <https://doi.org/10.1143/PTP.49.652>.
- [13] ATLAS Collaboration. “Direct top-quark decay width measurement in the $t\bar{t}$ lepton+jets channel at $\sqrt{s} = 8$ TeV with the ATLAS experiment.” In: *The European Physical Journal C* 78.2 (Feb. 2018). ISSN: 1434-6052. DOI: 10.1140/epjc/s10052-018-5595-5. URL: <http://dx.doi.org/10.1140/epjc/s10052-018-5595-5>.
- [14] CDF Collaboration. “Observation of single top quark production and measurement of $|V_{tb}|$ with CDF.” In: *Phys. Rev. D* 82 (11 Dec. 2010), p. 112005. DOI: 10.1103/PhysRevD.82.112005. URL: <https://link.aps.org/doi/10.1103/PhysRevD.82.112005>.
- [15] Michał Czakon, Paul Fiedler, and Alexander Mitov. “Total Top-Quark Pair-Production Cross Section at Hadron Colliders Through $\mathcal{O}(\alpha_S^4)$.” In: *Phys. Rev. Lett.* 110 (25 June 2013), p. 252004. DOI: 10.1103/PhysRevLett.110.252004. URL: <https://link.aps.org/doi/10.1103/PhysRevLett.110.252004>.
- [16] ATLAS Collaboration. *Search for s-Channel Single Top-Quark Production in pp Collisions at $\sqrt{s} = 7$ TeV*. Tech. rep. All figures including auxiliary figures are available at <https://atlas.web.cern.ch/Atlas/GROUPS/PHYSICS/CONFNOTES/ATLAS-CONF-2011-118>. Geneva: CERN, 2011. URL: <https://cds.cern.ch/record/1376410>.

- [17] ATLAS Collaboration. “Evidence for single top-quark production in the s-channel in proton–proton collisions at $\sqrt{s} = 7\text{ TeV}$ with the ATLAS detector using the Matrix Element Method.” In: *Physics Letters B* 756 (May 2016), pp. 228–246. ISSN: 0370-2693. DOI: 10.1016/j.physletb.2016.03.017. URL: <http://dx.doi.org/10.1016/j.physletb.2016.03.017>.
- [18] ATLAS Collaboration. “ATLAS experiment schematic or layout illustration.” General Photo. 2022. URL: <https://cds.cern.ch/record/2837191>.
- [19] Paolo Nason. “A New Method for Combining NLO QCD with Shower Monte Carlo Algorithms.” In: *Journal of High Energy Physics* 2004.11 (Nov. 2004), pp. 040–040. ISSN: 1029-8479. DOI: 10.1088/1126-6708/2004/11/040. URL: <http://dx.doi.org/10.1088/1126-6708/2004/11/040>.
- [20] Stefano Frixione, Paolo Nason, and Carlo Oleari. “Matching NLO QCD computations with parton shower simulations: the POWHEG method.” In: *Journal of High Energy Physics* 2007.11 (Nov. 2007), pp. 070–070. ISSN: 1029-8479. DOI: 10.1088/1126-6708/2007/11/070. URL: <http://dx.doi.org/10.1088/1126-6708/2007/11/070>.
- [21] Simone Alioli et al. “A general framework for implementing NLO calculations in shower Monte Carlo programs: the POWHEG BOX.” In: *Journal of High Energy Physics* 2010.6 (June 2010). ISSN: 1029-8479. DOI: 10.1007/jhep06(2010)043. URL: [http://dx.doi.org/10.1007/JHEP06\(2010\)043](http://dx.doi.org/10.1007/JHEP06(2010)043).
- [22] Christian Bierlich et al. *A comprehensive guide to the physics and usage of PYTHIA 8.3*. 2022. arXiv: 2203.11601 [hep-ph]. URL: <https://arxiv.org/abs/2203.11601>.
- [23] Bo Andersson. “THE LUND STRING MODEL.” In: *7th European Symposium on Antiproton Interactions: From LEAR to the Collider and Beyond*. 1986.
- [24] Andrew Buckley. “ATLAS Pythia 8 tunes to 7 TeV data.” In: *6th International Workshop on Multiple Partonic Interactions at the LHC*. Dec. 2014, p. 29.
- [25] Manuel Bähr et al. “Herwig++ physics and manual.” In: *The European Physical Journal C* 58.4 (Nov. 2008), pp. 639–707. ISSN: 1434-6052. DOI: 10.1140/epjc/s10052-008-0798-9. URL: <http://dx.doi.org/10.1140/epjc/s10052-008-0798-9>.
- [26] Johannes Bellm et al. “Herwig 7.0/Herwig++ 3.0 release note.” In: *The European Physical Journal C* 76.4 (Apr. 2016). ISSN: 1434-6052. DOI: 10.1140/epjc/s10052-016-4018-8. URL: <http://dx.doi.org/10.1140/epjc/s10052-016-4018-8>.

Bibliography

- [27] B.R. Webber. “A QCD model for jet fragmentation including soft gluon interference.” In: *Nuclear Physics B* 238.3 (1984), pp. 492–528. ISSN: 0550-3213. DOI: [https://doi.org/10.1016/0550-3213\(84\)90333-X](https://doi.org/10.1016/0550-3213(84)90333-X). URL: <https://www.sciencedirect.com/science/article/pii/055032138490333X>.
- [28] Enrico Bothmann et al. “Event generation with Sherpa 2.2.” In: *SciPost Phys.* 7 (2019), p. 034. DOI: 10.21468/SciPostPhys.7.3.034. URL: <https://scipost.org/10.21468/SciPostPhys.7.3.034>.
- [29] David J. Lange. “The EvtGen particle decay simulation package.” In: *Nuclear Instruments and Methods in Physics Research Section A: Accelerators, Spectrometers, Detectors and Associated Equipment* 462.1 (2001). BEAUTY2000, Proceedings of the 7th Int. Conf. on B-Physics at Hadron Machines, pp. 152–155. ISSN: 0168-9002. DOI: [https://doi.org/10.1016/S0168-9002\(01\)00089-4](https://doi.org/10.1016/S0168-9002(01)00089-4). URL: <https://www.sciencedirect.com/science/article/pii/S0168900201000894>.
- [30] Richard D. Ball et al. “Parton distributions for the LHC run II.” In: *Journal of High Energy Physics* 2015.4 (Apr. 2015). ISSN: 1029-8479. DOI: 10.1007/jhep04(2015)040. URL: [http://dx.doi.org/10.1007/JHEP04\(2015\)040](http://dx.doi.org/10.1007/JHEP04(2015)040).
- [31] Richard D. Ball et al. “Parton distributions with LHC data.” In: *Nuclear Physics B* 867.2 (Feb. 2013), pp. 244–289. ISSN: 0550-3213. DOI: 10.1016/j.nuclphysb.2012.10.003. URL: <http://dx.doi.org/10.1016/j.nuclphysb.2012.10.003>.
- [32] ATLAS Collaboration. “The ATLAS Simulation Infrastructure.” In: *The European Physical Journal C* 70.3 (Sept. 2010), pp. 823–874. ISSN: 1434-6052. DOI: 10.1140/epjc/s10052-010-1429-9. URL: <http://dx.doi.org/10.1140/epjc/s10052-010-1429-9>.
- [33] S. Agostinelli et al. “Geant4—a simulation toolkit.” In: *Nuclear Instruments and Methods in Physics Research Section A: Accelerators, Spectrometers, Detectors and Associated Equipment* 506.3 (2003), pp. 250–303. ISSN: 0168-9002. DOI: [https://doi.org/10.1016/S0168-9002\(03\)01368-8](https://doi.org/10.1016/S0168-9002(03)01368-8). URL: <https://www.sciencedirect.com/science/article/pii/S0168900203013688>.
- [34] ATLAS Collaboration. “Electron and photon performance measurements with the ATLAS detector using the 2015–2017 LHC proton-proton collision data.” In: *Journal of Instrumentation* 14.12 (Dec. 2019), P12006–P12006. ISSN: 1748-0221. DOI: 10.1088/1748-0221/14/12/p12006. URL: <http://dx.doi.org/10.1088/1748-0221/14/12/P12006>.

- [35] ATLAS Collaboration. “Muon reconstruction performance of the ATLAS detector in proton–proton collision data at $\sqrt{s} = 13$ TeV.” In: *The European Physical Journal C* 76.5 (May 2016). ISSN: 1434-6052. DOI: 10.1140/epjc/s10052-016-4120-y. URL: <http://dx.doi.org/10.1140/epjc/s10052-016-4120-y>.
- [36] Matteo Cacciari, Gavin P Salam, and Gregory Soyez. “The anti- k_t jet clustering algorithm.” In: *Journal of High Energy Physics* 2008.04 (Apr. 2008), pp. 063–063. ISSN: 1029-8479. DOI: 10.1088/1126-6708/2008/04/063. URL: <http://dx.doi.org/10.1088/1126-6708/2008/04/063>.
- [37] Matteo Cacciari, Gavin P. Salam, and Gregory Soyez. “FastJet user manual: (for version 3.0.2).” In: *The European Physical Journal C* 72.3 (Mar. 2012). ISSN: 1434-6052. DOI: 10.1140/epjc/s10052-012-1896-2. URL: <http://dx.doi.org/10.1140/epjc/s10052-012-1896-2>.
- [38] ATLAS Collaboration. *Tagging and suppression of pileup jets with the ATLAS detector*. Tech. rep. All figures including auxiliary figures are available at <https://atlas.web.cern.ch/Atlas/GROUPS/PHYSICS/CONFNOTES/ATLAS-CONF-2014-018>. Geneva: CERN, 2014. URL: <https://cds.cern.ch/record/1700870>.
- [39] ATLAS Collaboration. “Identification and rejection of pile-up jets at high pseudorapidity with the ATLAS detector.” In: *The European Physical Journal C* 77.9 (Sept. 2017). ISSN: 1434-6052. DOI: 10.1140/epjc/s10052-017-5081-5. URL: <http://dx.doi.org/10.1140/epjc/s10052-017-5081-5>.
- [40] ATLAS Collaboration. *Transforming jet flavour tagging at ATLAS*. 2025. arXiv: 2505.19689 [hep-ex]. URL: <https://arxiv.org/abs/2505.19689>.
- [41] ATLAS Collaboration. “ATLAS b-jet identification performance and efficiency measurement with $t\bar{t}$ events in pp collisions at $\sqrt{s} = 13$ TeV.” In: *The European Physical Journal C* 79.11 (Nov. 2019). ISSN: 1434-6052. DOI: 10.1140/epjc/s10052-019-7450-8. URL: <http://dx.doi.org/10.1140/epjc/s10052-019-7450-8>.
- [42] ATLAS Collaboration. *Measurement of b-tagging Efficiency of c-jets in $t\bar{t}$ Events Using a Likelihood Approach with the ATLAS Detector*. Tech. rep. All figures including auxiliary figures are available at <https://atlas.web.cern.ch/Atlas/GROUPS/PHYSICS/CONFNOTES/ATLAS-CONF-2018-001>. Geneva: CERN, 2018. URL: <https://cds.cern.ch/record/2306649>.
- [43] ATLAS Collaboration. *Calibration of light-flavour b-jet mistagging rates using ATLAS proton-proton collision data at $\sqrt{s} = 13$ TeV*. Tech. rep. All figures including auxiliary figures are available at <https://atlas.web.cern.ch/Atlas/GROUPS/PHYSICS/CONFNOTES/ATLAS-CONF-2018-002>.

Bibliography

- las/GROUPS/PHYSICS/CONFNOTES/ATLAS-CONF-2018-006. Geneva: CERN, 2018. URL: <https://cds.cern.ch/record/2314418>.
- [44] Niklas Düser. *Search for single top quark production at ATLAS using Deep Neural Networks and Graph Neural Networks*. Master's Thesis. Sept. 2025.
- [45] François Chollet. *Keras API*. 2015. URL: <https://keras.io/>.
- [46] Martín Abadi et al. *TensorFlow: Large-Scale Machine Learning on Heterogeneous Distributed Systems*. Software available from tensorflow.org. 2016. arXiv: 1603.04467 [cs.DC]. URL: <https://arxiv.org/abs/1603.04467>.
- [47] Diederik P. Kingma and Jimmy Ba. *Adam: A Method for Stochastic Optimization*. 2017. arXiv: 1412.6980 [cs.LG]. URL: <https://arxiv.org/abs/1412.6980>.
- [48] Kyle Cranmer et al. *HistFactory: A tool for creating statistical models for use with RooFit and RooStats*. Tech. rep. New York: New York U., 2012. DOI: 10.17181/CERN-OPEN-2012-016. URL: <https://cds.cern.ch/record/1456844>.
- [49] F. James and M. Roos. “Minuit - a system for function minimization and analysis of the parameter errors and correlations.” In: *Computer Physics Communications* 10.6 (1975), pp. 343–367. ISSN: 0010-4655. DOI: [https://doi.org/10.1016/0010-4655\(75\)90039-9](https://doi.org/10.1016/0010-4655(75)90039-9). URL: <https://www.sciencedirect.com/science/article/pii/0010465575900399>.
- [50] ATLAS Collaboration. *Studies on the improvement of the matching uncertainty definition in top-quark processes simulated with Powheg+Pythia 8*. Tech. rep. All figures including auxiliary figures are available at <https://atlas.web.cern.ch/Atlas/GROUPS/PHYSICS/PUBNOTES/ATL-PHYS-PUB-2023-029>. Geneva: CERN, 2023. URL: <https://cds.cern.ch/record/2872787>.
- [51] ATLAS Collaboration. “Luminosity determination in pp collisions at $\sqrt{s} = 13\text{ TeV}$ using the ATLAS detector at the LHC.” In: *The European Physical Journal C* 83.10 (Oct. 2023). ISSN: 1434-6052. DOI: 10.1140/epjc/s10052-023-11747-w. URL: <http://dx.doi.org/10.1140/epjc/s10052-023-11747-w>.
- [52] Andrés Pinto et al. *Uncertainty components in profile likelihood fits*. 2024. arXiv: 2307.04007 [physics.data-an]. URL: <https://arxiv.org/abs/2307.04007>.

Eidesstattliche Versicherung

(Affidavit)

Name, Vorname
(surname, first name)

Bachelorarbeit
(Bachelor's thesis)

Titel
(Title)

Matrikelnummer
(student ID number)

Masterarbeit
(Master's thesis)

Ich versichere hiermit an Eides statt, dass ich die vorliegende Abschlussarbeit mit dem oben genannten Titel selbstständig und ohne unzulässige fremde Hilfe erbracht habe. Ich habe keine anderen als die angegebenen Quellen und Hilfsmittel benutzt sowie wörtliche und sinngemäße Zitate kenntlich gemacht. Die Arbeit hat in gleicher oder ähnlicher Form noch keiner Prüfungsbehörde vorgelegen.

I declare in lieu of oath that I have completed the present thesis with the above-mentioned title independently and without any unauthorized assistance. I have not used any other sources or aids than the ones listed and have documented quotations and paraphrases as such. The thesis in its current or similar version has not been submitted to an auditing institution before.

Ort, Datum
(place, date)

Unterschrift
(signature)

Belehrung:

Wer vorsätzlich gegen eine die Täuschung über Prüfungsleistungen betreffende Regelung einer Hochschulprüfungsordnung verstößt, handelt ordnungswidrig. Die Ordnungswidrigkeit kann mit einer Geldbuße von bis zu 50.000,00 € geahndet werden. Zuständige Verwaltungsbehörde für die Verfolgung und Ahndung von Ordnungswidrigkeiten ist der Kanzler/die Kanzlerin der Technischen Universität Dortmund. Im Falle eines mehrfachen oder sonstigen schwerwiegenden Täuschungsversuches kann der Prüfling zudem exmatrikuliert werden. (§ 63 Abs. 5 Hochschulgesetz - HG -).

Die Abgabe einer falschen Versicherung an Eides statt wird mit Freiheitsstrafe bis zu 3 Jahren oder mit Geldstrafe bestraft.

Die Technische Universität Dortmund wird ggf. elektronische Vergleichswerkzeuge (wie z.B. die Software „turnitin“) zur Überprüfung von Ordnungswidrigkeiten in Prüfungsverfahren nutzen.

Die oben stehende Belehrung habe ich zur Kenntnis genommen:

Official notification:

Any person who intentionally breaches any regulation of university examination regulations relating to deception in examination performance is acting improperly. This offense can be punished with a fine of up to EUR 50,000.00. The competent administrative authority for the pursuit and prosecution of offenses of this type is the Chancellor of TU Dortmund University. In the case of multiple or other serious attempts at deception, the examinee can also be unenrolled, Section 63 (5) North Rhine-Westphalia Higher Education Act (*Hochschulgesetz, HG*).

The submission of a false affidavit will be punished with a prison sentence of up to three years or a fine.

As may be necessary, TU Dortmund University will make use of electronic plagiarism-prevention tools (e.g. the "turnitin" service) in order to monitor violations during the examination procedures.

I have taken note of the above official notification.*

Ort, Datum
(place, date)

Unterschrift
(signature)

***Please be aware that solely the German version of the affidavit ("Eidesstattliche Versicherung") for the Bachelor's/ Master's thesis is the official and legally binding version.**